Target Localization Methods Based on Iterative Super-Resolution for Bistatic MIMO Radar

Jianhe Du *[ID], **Meng Han**[ID], **Libiao Jin, Yan Hua and Shufeng Li**

School of Information and Communication Engineering, Communication University of China, Beijing 100024, China; hm593@cuc.edu.cn (M.H.); libiao@cuc.edu.cn (L.J.); huayan@cuc.edu.cn (Y.H.); lishufeng@cuc.edu.cn (S.L.)
* Correspondence: dujianhe1@gmail.com

check for updates

Abstract: The direction-of-departure (DOD) and the direction-of-arrival (DOA) are important localization parameters in bistatic MIMO radar. In this paper, we are interested in DOD/DOA estimation of both single-pulse and multiple-pulse multiple-input multiple-output (MIMO) radars. An iterative super-resolution target localization method is firstly proposed for single-pulse bistatic MIMO radar. During the iterative process, the estimated DOD and DOA can be moved from initial angles to their true values with high probability, and thus can achieve super-resolution estimation. It works well even if the number of targets is unknown. We then extend the proposed method to multiple-pulse configuration to estimate target numbers and localize targets. Compared with existing methods, both of our proposed algorithms have a higher localization accuracy and a more stable performance. Moreover, the proposed algorithms work well even with low sampling numbers and unknown target numbers. Simulation results demonstrate the effectiveness of the proposed methods.

Keywords: MIMO radar; target localization; super-resolution; DOD/DOA; unknown target numbers

1. Introduction

A multiple-input multiple-output (MIMO) technique [1–4] can improve the spectral efficiency and transmission rate without increasing transmitting power. It has been one of the most critical techniques in 4th-generation (4G) wireless communication systems. MIMO radars [5–7] combine MIMO and digital array techniques. They are capacitated to simultaneously transmit and receive linearly independent signals [8,9] by using multiple antennas. The correlation coefficient of waveforms is an important parameter representing the degree of this waveform diversity. The correlation coefficient of the orthogonal waveform MIMO radar is equal to zero, which means that all waveforms are orthogonal to each other. That of the phased array radar is equal to one, which means that all waveforms are identical. Similarly, for partial correlation waveform MIMO radar, its correlation coefficient is between zero and one. Compared with traditional phased-array radars, MIMO radars can estimate more targets with higher detection accuracy, which has attracted attention in recent years.

The direction-of-departure (DOD) and the direction-of-arrival (DOA) [10–12] are important parameters in bistatic MIMO radars. In this paper, we consider two types of bistatic MIMO radars, which correspond to single-pulse and multiple-pulse configurations, respectively.

There are many DOD/DOA estimation methods based on radar-imaging techniques, such as Capon [13,14] and MUSIC [11,15,16] algorithms. The two-dimensional (2D) Capon (2D-Capon) and 2D MUSIC (2D-MUSIC) methods localize targets via scanning their 2D output spectra and looking for peaks in a range of interested angles. In [13], a reduced-dimension Capon (RD-Capon) algorithm is proposed in bistatic MIMO radar, which can estimate DODs/DOAs by a one-dimensional (1D) search. The paper [14] is an extended version of [13], which realizes the automatic pairing of DODs

and DOAs. A reduced-dimension MUSIC (RD-MUSIC) algorithm is proposed in [11] for localizing targets. It also only requires the 1D search and pairs automatically. Compared with a 2D search, the complexity of reduced-dimension algorithms is reduced. The paper [16] combines beam-space processing and reduced-dimension transformation for monostatic MIMO radar localization in order to further alleviate the computational burden. However, their angular resolution is still dominated by the scanning step size, and a small step size leads to high complexity. Therefore, the localization methods based on 1D or 2D radar-imaging techniques may be significantly time-consuming for high angular resolution cases.

ESPRIT [17–19] is also a commonly used target localization algorithm with high resolution and high efficiency. It utilizes the rotational invariance of the signal subspace, which is caused by the shift invariance of the transmit and receive antenna arrays. In [18], a unitary ESPRIT algorithm using the real-valued signal matrix transformed by the received data matrix is developed for bistatic MIMO radar for target localization. It can achieve automatic angle pairing and has lower complexity than the ESPRIT method in [17]. The paper [19] puts forward a ESPRIT-like method suitable for the coexistence of circular and noncircular signals in bistatic MIMO radar.

However, a growing number of scenarios allows signals to be represented in the form of tensors, i.e., multidimensional matrices. Tensor-based decomposition frameworks such as parallel factor (PARAFAC) decomposition and Tucker decomposition, which make full use of the strong algebraic structure of multidimensional signals, are widely used for MIMO radar target localization [20–22]. The paper [21] shows a tensor-based real-valued subspace scheme, which combines the higher order singular value decomposition (HOSVD) technique with the methods based on real-valued subspace to estimate DODs and DOAs. In [22], a unitary PARAFAC method based on the transmit beam-space is proposed for bistatic MIMO radar. These tensor-based methods enhance the estimation performance to some degree. However, they are only applicable to multiple-pulse radar configuration and thus are limited in application scope.

Recently, a novel compressed sensing method was proposed in [23] for 1D line spectral estimation. It utilizes the iterative reweighted (IR) scheme for sparse signal recovery. In [24], the IR scheme in [23] is extended to 2D millimeter-Wave (mmWave) channel estimation, and achieves higher channel estimation accuracy than conventional solutions.

Inspired by the idea of the IR algorithm, we firstly propose a new super-resolution target localization method for single-pulse bistatic MIMO radar, which can be abbreviated as the ISR-S method. It does not require extra angle pairing. We then develop it to multiple-pulse radar in an effort to initialize the trilinear alternate least squares (TALS) algorithm for estimating target numbers and localizing targets, i.e., the proposed ISR-M algorithm. In this configuration, due to the superior angle estimation performance of the proposed ISR-S algorithm, it demonstrates better localization performance than Capon and MUSIC algorithms at a low signal-to-noise ratio (SNR) even when only one pulse-period-received signal is utilized to localize targets.

Our contributions are as follows.

(1) Compared with existing Capon, MUSIC, and ESPRIT methods, both of the proposed ISR-S and ISR-M methods have better angle estimation performance in single-pulse and multiple-pulse scenarios, respectively.

(2) Since the proposed ISR-M method optimizes the initial values before the alternately iterative process, it has a more stable performance and a faster convergence speed. The average iteration number of the ISR-M method is reduced by nearly half compared with the traditional TALS algorithm.

(3) In contrast to tensor-based methods in [20–22], the two proposed schemes do not need to transmit mutually orthogonal waveforms. In addition, the proposed ISR-M method has more easy uniqueness conditions than the algorithm in [20].

(4) Traditional Capon, MUSIC, ESPRIT, and TALS methods cannot effectively localize targets when the number of targets is unknown. However, both of the proposed ISR-S and ISR-M methods not only can perform localization in this case, but also have high localization accuracy.

The remainder of this paper is organized as follows. In Section 2, we present the considered single-pulse bistatic MIMO radar model in detail and derive the optimization formulas. Besides, the proposed ISR-S algorithm for target localization is also given in this section. In Section 3, we present the considered multiple-pulse bistatic MIMO radar model and the constructed tensor model. In addition, the ISR-M algorithm is also introduced in this section. Section 4 shows simulation results to verify the performance of our two proposed methods. Conclusions are drawn in Section 5.

Notation: $(\cdot)^{\mathrm{T}}$, $(\cdot)^{\mathrm{H}}$, and $(\cdot)^{-1}$ represent the transpose, the conjugate transpose, and the inverse-operation, respectively. $\mathrm{diag}\,(\cdot)$ is a diagonal matrix whose diagonal elements are the entries of a vector. $\mathrm{vec}\,(\cdot)$ is a vector obtained by stacking the columns of a matrix one after another. $D_i\,(\mathbf{A})$ is a diagonal matrix formed by the *i*-th row of $\mathbf{A}$. The notation $\otimes$, $\odot$, and $\circ$ stand for the Kronecker product, the Khatri-Rao product (or the column-wise Kronecker product), and the outer product, respectively. The $N \times N$ identity matrix is denoted by $\mathbf{I}_N$. The l_0-norm and l_2-norm are denoted by $\|\cdot\|_0$ and $\|\cdot\|_2$, respectively.

2. Single-Pulse Bistatic MIMO Radar

2.1. System Model

Figure 1 shows a bistatic MIMO radar system model. In this subsection, we consider a single-pulse bistatic radar consisting of M_T transmit antennas and M_R receive antennas. Transmit and receive arrays considered in this paper are all uniform linear arrays (ULAs) with half-wavelength spacing. Each target is treated as a point-source in the far field as described in existing works [18,20]. The transmit steering vector and the receive steering vector can be respectively written as

$$
\begin{aligned}
\mathbf{a}_\mathrm{T}(\phi_{\mathrm{T},k}) &= \left[\; 1 \quad \exp\left((-j\tfrac{2\pi}{\lambda})d\sin\phi_{\mathrm{T},k}\right) \quad \cdots \quad \exp\left((-j\tfrac{2\pi}{\lambda})d(M_\mathrm{T}-1)\sin\phi_{\mathrm{T},k}\right) \;\right]^{\mathrm{T}} \in \mathbb{C}^{M_\mathrm{T}\times 1}, \\
\mathbf{a}_\mathrm{R}(\phi_{\mathrm{R},k}) &= \left[\; 1 \quad \exp\left((-j\tfrac{2\pi}{\lambda})d\sin\phi_{\mathrm{R},k}\right) \quad \cdots \quad \exp\left((-j\tfrac{2\pi}{\lambda})d(M_\mathrm{R}-1)\sin\phi_{\mathrm{R},k}\right) \;\right]^{\mathrm{T}} \in \mathbb{C}^{M_\mathrm{R}\times 1}
\end{aligned}
\tag{1}
$$

where K is the number of targets in a range-bin of interests, $\phi_{\mathrm{T},k}$ and $\phi_{\mathrm{R},k}$ are DOD and DOA, respectively, $k = 1, \cdots, K$, d is the spacing of two adjacent antennas, and λ is the wavelength.
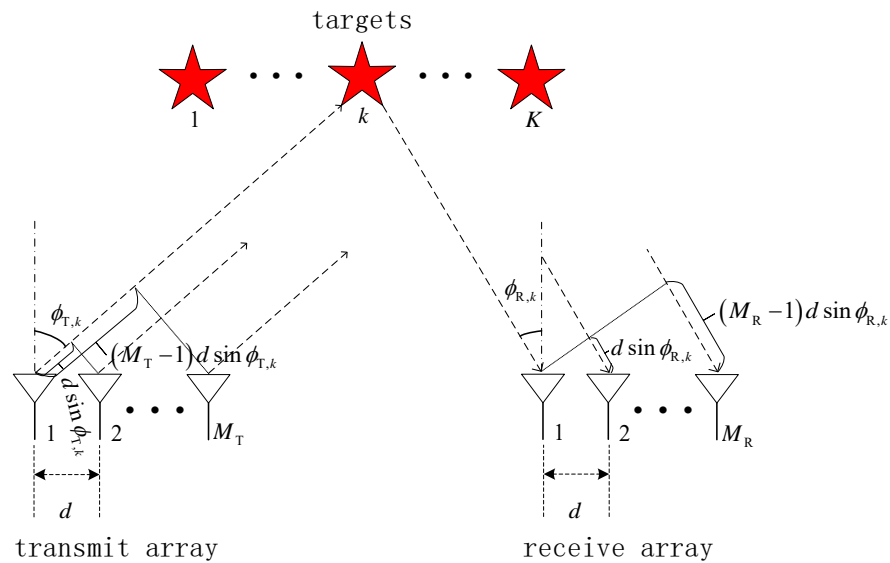

Figure 1. Schematic illustration of the considered bistatic MIMO radar.

The signals matrix is first transmitted by the transmit antenna array and then reflected by the targets. The reflected waveform vector with DOD $\phi_{\mathrm{T},k}$ is $\mathbf{a}_\mathrm{T}^{\mathrm{T}}(\phi_{\mathrm{T},k})\mathbf{S}$, in which $\mathbf{S} = \left[\mathbf{s}_1, \mathbf{s}_2, \cdots, \mathbf{s}_{M_\mathrm{T}}\right]^{\mathrm{T}} \in$

$\mathbb{C}^{M_T \times L}$ is the transmitted waveform matrix, and L is the number of samples. Therefore, the signals reflected from targets with different DODs are linearly independent. The signals matrix is then received by M_R receive antennas, which can be expressed as

$$\mathbf{Y} = \sum_{k=1}^{K} \beta_k \mathbf{a}_R(\phi_{R,k}) \mathbf{a}_T^T(\phi_{T,k}) \mathbf{S} + \mathbf{V} \tag{2}$$

where β_k is the radar cross section (RCS) fading coefficient, and $\mathbf{V} \in \mathbb{C}^{M_R \times L}$ is the additive Gaussian white noise (AWGN) matrix.

By defining $\theta_{T,k} = d \sin \phi_{T,k}/\lambda$ and $\theta_{R,k} = d \sin \phi_{R,k}/\lambda$ as the normalized spacial angles, the transmit and receive steering matrices can be expressed as

$$\begin{aligned}
\mathbf{A}_T(\theta_T) &= \begin{bmatrix} \mathbf{a}_T(\theta_{T,1}) & ... & \mathbf{a}_T(\theta_{T,K}) \end{bmatrix} \in \mathbb{C}^{M_T \times K}, \\
\mathbf{A}_R(\theta_R) &= \begin{bmatrix} \mathbf{a}_R(\theta_{R,1}) & ... & \mathbf{a}_R(\theta_{R,K}) \end{bmatrix} \in \mathbb{C}^{M_R \times K}
\end{aligned} \tag{3}$$

where $\theta_T = \begin{bmatrix} \theta_{T,1} & \cdots & \theta_{T,K} \end{bmatrix}^T$ and $\theta_R = \begin{bmatrix} \theta_{R,1} & \cdots & \theta_{R,K} \end{bmatrix}^T$. Then, (2) can be expressed equivalently as follows [25,26]:

$$\mathbf{Y} = \mathbf{A}_R(\theta_R) \operatorname{diag}(\mathbf{c}) \mathbf{A}_T^T(\theta_T) \mathbf{S} + \mathbf{V} \tag{4}$$

where $\mathbf{c} = \begin{bmatrix} \beta_1 & \cdots & \beta_K \end{bmatrix}^T \in \mathbb{C}^{K \times 1}$. After vectoring Equation (4), we obtain

$$\mathbf{y} = (\mathbf{S}^T \otimes \mathbf{I}_{M_R}) (\mathbf{A}_T(\theta_T) \odot \mathbf{A}_R(\theta_R)) \mathbf{c} + \mathbf{v} \tag{5}$$

where $\mathbf{y} \in \mathbb{C}^{LM_R \times 1}$ and $\mathbf{v} \in \mathbb{C}^{LM_R \times 1}$.

2.2. Optimization Formulas

The target localization problem of this single-pulse bistatic MIMO radar can be formulated as

$$\min_{\hat{\mathbf{c}}, \hat{\theta}_T, \hat{\theta}_R} \|\hat{\mathbf{c}}\|_0, \quad \text{s.t.} \left\| \mathbf{y} - (\mathbf{S}^T \otimes \mathbf{I}_{M_R}) (\mathbf{A}_T(\hat{\theta}_T) \odot \mathbf{A}_R(\hat{\theta}_R)) \hat{\mathbf{c}} \right\|_2 \leqslant \varepsilon \tag{6}$$

where $\hat{\mathbf{c}}$ is the estimated RCS fading coefficient vector, $\|\hat{\mathbf{c}}\|_0$ represents the estimated number of targets, $\hat{\theta}_R$ and $\hat{\theta}_T$ are the estimation of the normalized spacial angles, and ε is the error tolerance parameter. Equation (6) can be transformed into the following log-sum function [23,27,28]:

$$\min_{\hat{\mathbf{c}}, \hat{\theta}_T, \hat{\theta}_R} G(\mathbf{c}) = \sum_{k=1}^{K} \log\left(\left|\hat{\beta}_k\right|^2 + \delta\right), \quad \text{s.t.} \left\| \mathbf{y} - (\mathbf{S}^T \otimes \mathbf{I}_{M_R}) (\mathbf{A}_T(\hat{\theta}_T) \odot \mathbf{A}_R(\hat{\theta}_R)) \hat{\mathbf{c}} \right\|_2 \leqslant \varepsilon \tag{7}$$

where $\delta > 0$ makes sure the function is well-defined. We then introduce a regularization parameter α and have

$$\min_{\hat{\mathbf{c}}, \hat{\theta}_T, \hat{\theta}_R} P(\mathbf{c}, \theta_T, \theta_R) = \sum_{k=1}^{K} \log\left(\left|\hat{\beta}_k\right|^2 + \delta\right) + \alpha \left\| \mathbf{y} - (\mathbf{S}^T \otimes \mathbf{I}_{M_R}) (\mathbf{A}_T(\hat{\theta}_T) \odot \mathbf{A}_R(\hat{\theta}_R)) \hat{\mathbf{c}} \right\|_2^2. \tag{8}$$

We further use the following iterative surrogate function instead of the above formula for angle estimation

$$\min_{\hat{\mathbf{c}}, \hat{\theta}_T, \hat{\theta}_R} R^{(i)}(\mathbf{c}, \theta_T, \theta_R) = \alpha^{-1} \hat{\mathbf{c}}^H \mathbf{\Sigma}^{(i)} \hat{\mathbf{c}} + \left\| \mathbf{y} - (\mathbf{S}^T \otimes \mathbf{I}_{M_R}) (\mathbf{A}_T(\hat{\theta}_T) \odot \mathbf{A}_R(\hat{\theta}_R)) \hat{\mathbf{c}} \right\|_2^2 \tag{9}$$

where

$$\boldsymbol{\Sigma}^{(i)} = \mathrm{diag}\left(\rho_1, \cdots, \rho_K\right), \tag{10}$$

and $\rho_k = \frac{1}{\left|\hat{\beta}_k^{(i)}\right|^2 + \delta}$.

2.3. Localization via the Proposed ISR-S Method

Firstly, we simplify $R^{(i)}\left(\mathbf{c}, \theta_\mathrm{T}, \theta_\mathrm{R}\right)$ as follows

$$
\begin{aligned}
R^{(i)}(\mathbf{c}, \theta_\mathrm{T}, \theta_\mathrm{R}) &= \alpha^{-1}\hat{\mathbf{c}}^\mathrm{H}\boldsymbol{\Sigma}^{(i)}\hat{\mathbf{c}} + (\mathbf{y} - \mathbf{F}\hat{\mathbf{c}})^\mathrm{H}(\mathbf{y} - \mathbf{F}\hat{\mathbf{c}}) \\
&= \alpha^{-1}\hat{\mathbf{c}}^\mathrm{H}\boldsymbol{\Sigma}^{(i)}\hat{\mathbf{c}} + \mathbf{y}^\mathrm{H}\mathbf{y} - \mathbf{y}^\mathrm{H}\mathbf{F}\hat{\mathbf{c}} - \hat{\mathbf{c}}^\mathrm{H}\mathbf{F}^\mathrm{H}\mathbf{y} + \hat{\mathbf{c}}^\mathrm{H}\mathbf{F}^\mathrm{H}\mathbf{F}\hat{\mathbf{c}} \\
&= \hat{\mathbf{c}}^\mathrm{H}\mathbf{W}\hat{\mathbf{c}} - \hat{\mathbf{c}}^\mathrm{H}\mathbf{F}^\mathrm{H}\mathbf{y} - \mathbf{y}^\mathrm{H}\mathbf{F}\hat{\mathbf{c}} + \mathbf{y}^\mathrm{H}\mathbf{y}
\end{aligned}
\tag{11}
$$

with

$$
\begin{aligned}
\mathbf{F} &= \left(\mathbf{S}^\mathrm{T} \otimes \mathbf{I}_{M_\mathrm{R}}\right)\left(\mathbf{A}_\mathrm{T}\left(\hat{\theta}_\mathrm{T}\right) \odot \mathbf{A}_\mathrm{R}\left(\hat{\theta}_\mathrm{R}\right)\right) \\
&= \left(\mathbf{S}^\mathrm{T} \otimes \mathbf{I}_{M_\mathrm{R}}\right)\left[\begin{array}{ccc} \mathrm{vec}\left(\mathbf{a}_{\mathrm{R},1}\mathbf{a}_{\mathrm{T},1}^\mathrm{T}\right) & \cdots & \mathrm{vec}\left(\mathbf{a}_{\mathrm{R},K}\mathbf{a}_{\mathrm{T},K}^\mathrm{T}\right) \end{array}\right]
\end{aligned}
\tag{12}
$$

and

$$\mathbf{W} = \alpha^{-1}\boldsymbol{\Sigma}^{(i)} + \mathbf{F}^\mathrm{H}\mathbf{F}. \tag{13}$$

We then derive the following partial derivative with regard to $\mathbf{c}$

$$\frac{\partial R^{(i)}(\mathbf{c}, \theta_\mathrm{T}, \theta_\mathrm{R})}{\partial \mathbf{c}} = \hat{\mathbf{c}}^\mathrm{H}\mathbf{W} - \mathbf{y}^\mathrm{H}\mathbf{F}. \tag{14}$$

After setting Equation (14) to zero, we obtain the optimal $\hat{\mathbf{c}}^{(i)}$ and the corresponding optimal value of $R^{(i)}$ as follows:

$$
\begin{aligned}
\mathbf{c}_\mathrm{opt}^{(i)}\left(\theta_\mathrm{T}, \theta_\mathrm{R}\right) &= \arg\min_{\mathbf{c}} R^{(i)}(\mathbf{c}, \theta_\mathrm{T}, \theta_\mathrm{R}) \\
&= \mathbf{W}^{-1}\mathbf{F}^\mathrm{H}\mathbf{y}
\end{aligned}
\tag{15}
$$

$$
\begin{aligned}
R_\mathrm{opt}^{(i)}(\theta_\mathrm{T}, \theta_\mathrm{R}) &= \min_{\mathbf{c}} R^{(i)}(\mathbf{c}, \theta_\mathrm{T}, \theta_\mathrm{R}) \\
&= \mathbf{y}^\mathrm{H}\mathbf{y} - \mathbf{y}^\mathrm{H}\mathbf{F}\mathbf{W}^{-1}\mathbf{F}^\mathrm{H}\mathbf{y}.
\end{aligned}
\tag{16}
$$

After that, the normalized spatial angles θ_T and θ_R are optimized by using the gradient descent method as follows:

$$
\begin{aligned}
\theta_\mathrm{T}^{(i+1)} &= \theta_\mathrm{T}^{(i)} - \eta\nabla_{\theta_\mathrm{T}}R_\mathrm{opt}^{(i)}\left(\theta_\mathrm{T}^{(i)}, \theta_\mathrm{R}^{(i)}\right), \\
\theta_\mathrm{R}^{(i+1)} &= \theta_\mathrm{R}^{(i)} - \eta\nabla_{\theta_\mathrm{R}}R_\mathrm{opt}^{(i)}\left(\theta_\mathrm{T}^{(i)}, \theta_\mathrm{R}^{(i)}\right)
\end{aligned}
\tag{17}
$$

where η is the chosen step size to ensure $\hat{R}_\mathrm{opt}^{(i+1)}\left(\theta_\mathrm{T}, \theta_\mathrm{R}\right) \leqslant \hat{R}_\mathrm{opt}^{(i)}\left(\theta_\mathrm{T}, \theta_\mathrm{R}\right)$, $\nabla_{\theta_\mathrm{T}}R_\mathrm{opt}^{(i)}\left(\theta_\mathrm{T}^{(i)}, \theta_\mathrm{R}^{(i)}\right)$, and $\nabla_{\theta_\mathrm{R}}R_\mathrm{opt}^{(i)}\left(\theta_\mathrm{T}^{(i)}, \theta_\mathrm{R}^{(i)}\right)$ are gradient functions upon θ_T and θ_R, respectively.

We take $\nabla_{\theta_\mathrm{T}}R_\mathrm{opt}^{(i)}\left(\theta_\mathrm{T}^{(i)}, \theta_\mathrm{R}^{(i)}\right)$ as an example for analysis and replace $R_\mathrm{opt}^{(i)}\left(\theta_\mathrm{T}^{(i)}, \theta_\mathrm{R}^{(i)}\right)$ with R_opt for notational brevity. After taking partial derivative with regard to $\theta_{\mathrm{T},k}$, we have

$$
\begin{aligned}
\frac{\partial R_\mathrm{opt}}{\partial \theta_{\mathrm{T},k}} &= -\mathbf{y}^\mathrm{H}\frac{\partial \mathbf{F}}{\partial \theta_{\mathrm{T},k}}\mathbf{W}^{-1}\mathbf{F}^\mathrm{H}\mathbf{y} - \mathbf{y}^\mathrm{H}\mathbf{F}\frac{\partial \mathbf{W}^{-1}}{\partial \theta_{\mathrm{T},k}}\mathbf{F}^\mathrm{H}\mathbf{y} - \mathbf{y}^\mathrm{H}\mathbf{F}\mathbf{W}^{-1}\frac{\partial \mathbf{F}^\mathrm{H}}{\partial \theta_{\mathrm{T},k}}\mathbf{y} \\
&= -\mathbf{y}^\mathrm{H}\frac{\partial \mathbf{F}}{\partial \theta_{\mathrm{T},k}}\mathbf{W}^{-1}\mathbf{F}^\mathrm{H}\mathbf{y} + \mathbf{y}^\mathrm{H}\mathbf{F}\mathbf{W}^{-1}\frac{\partial \mathbf{W}}{\partial \theta_{\mathrm{T},k}}\mathbf{W}^{-1}\mathbf{F}^\mathrm{H}\mathbf{y} - \mathbf{y}^\mathrm{H}\mathbf{F}\mathbf{W}^{-1}\frac{\partial \mathbf{F}^\mathrm{H}}{\partial \theta_{\mathrm{T},k}}\mathbf{y}
\end{aligned}
\tag{18}
$$

where

$$\frac{\partial \mathbf{W}}{\partial \theta_{\mathrm{T},k}} = \frac{\partial \mathbf{F}^\mathrm{H}}{\partial \theta_{\mathrm{T},k}}\mathbf{F} + \mathbf{F}^\mathrm{H}\frac{\partial \mathbf{F}}{\partial \theta_{\mathrm{T},k}} \tag{19}$$

and

$$\frac{\partial \mathbf{F}}{\partial \theta_{\mathrm{T},k}} = \left(\mathbf{S}^{\mathrm{T}} \otimes \mathbf{I}_{M_{\mathrm{R}}}\right) \begin{bmatrix} \mathbf{0} & \cdots & \mathbf{0} & \mathrm{vec}\left(\mathbf{a}_{\mathrm{R},1} \frac{\partial \mathbf{a}_{\mathrm{T},1}^{\mathrm{T}}}{\partial \theta_{\mathrm{T},k}}\right) & \mathbf{0} & \cdots & \mathbf{0} \end{bmatrix}. \tag{20}$$

The proposed iterative super-resolution target localization algorithm is summarized as Algorithm 1. In order to speed up the convergence of the algorithm, the singular value decomposition (SVD) [24] can be used to initialize $\hat{\theta}_{\mathrm{T}}^{(0)}$ and $\hat{\theta}_{\mathrm{R}}^{(0)}$. In **Step 7**, we regard $\hat{\beta}_k$ as noise and prune it if it is too small during the iteration process. Alternatively, **Step 7** can be omitted if the number of targets is given beforehand. Correspondingly, the initial value K_{init} is fixed to K. More specifically, we calculate the estimation error

$$e^{(i)} = \left\| \hat{\theta}_{\mathrm{T}}^{(i+1)} - \hat{\theta}_{\mathrm{T}}^{(i)} \right\|_2 + \left\| \hat{\theta}_{\mathrm{R}}^{(i+1)} - \hat{\theta}_{\mathrm{R}}^{(i)} \right\|_2 \tag{21}$$

in the i-th iteration, and we assume that the convergence condition is reached when $e^{(i)} \leqslant e_{\mathrm{th}}$.

Algorithm 1 The proposed ISR-S algorithm

Input: y and **S**.
Step 1 Initialization: Set $i = 0$; Initialize the target numbers K_{init} to ensure $K < K_{\mathrm{init}}$; Initialize $\hat{\theta}_{\mathrm{T}}^{(0)}, \hat{\theta}_{\mathrm{R}}^{(0)}$; Initialize $\hat{\mathfrak{c}}^{(0)}$ and $\hat{R}^{(0)}$ by Equations (15) and (16), respectively;
Step 2 $i = i + 1$;
Step 3 Calculate $\nabla_{\theta_{\mathrm{T}}} R_{\mathrm{opt}}^{(i)}\left(\theta_{\mathrm{T}}^{(i)}, \theta_{\mathrm{R}}^{(i)}\right)$ and $\nabla_{\theta_{\mathrm{R}}} R_{\mathrm{opt}}^{(i)}\left(\theta_{\mathrm{T}}^{(i)}, \theta_{\mathrm{R}}^{(i)}\right)$;
Step 4 Update the angle estimation $\hat{\theta}_{\mathrm{T}}^{(i)}$ and $\hat{\theta}_{\mathrm{R}}^{(i)}$ using Equation (17);
Step 5 Update $\hat{\mathfrak{c}}^{(i)}$ and $\hat{R}^{(i)}$ by Equations (15) and (16), respectively;
Step 6 Repeat **Step 2** to **Step 6** until convergence;
Step 7 Prune $\hat{\beta}_k$ when $\hat{\beta}_k < \beta_{\mathrm{th}}$, where β_{th} is a threshold.
Output: $\hat{K}$, $\hat{\theta}_{\mathrm{T}}$, $\hat{\theta}_{\mathrm{R}}$, and $\hat{\mathfrak{c}}$.

---

3. Extension to Localize Targets in Multiple-Pulse Bistatic MIMO Radar

In this subsection, we consider a multiple-pulse bistatic radar model, i.e., the coherent processing interval (CPI) consists of Q ($Q \geqslant 2$) pulses. It is assumed that the transmit and receive steering matrices do not vary with pulses. In the q-th pulse period, the L reflected sample signals observed by all M_{R} receive antennas can be expressed as

$$\mathbf{Y}_q = \sum_{k=1}^{K} \chi_{qk} \mathbf{a}_{\mathrm{R}}(\phi_{\mathrm{R},k}) \mathbf{a}_{\mathrm{T}}^{\mathrm{T}}(\phi_{\mathrm{T},k}) \mathbf{S}_q + \mathbf{V}_q \tag{22}$$

where χ_{qk} is a composite coefficient consisting of Doppler shift and RCS fading effects. $\mathbf{S}_q \in \mathbb{C}^{M_{\mathrm{T}} \times L}$ and $\mathbf{V}_q \in \mathbb{C}^{M_{\mathrm{R}} \times L}$ are the transmitted waveform matrix and the AWGN matrix in the q-th pulse period, respectively. In the multiple-pulse configuration, χ_{qk} has two forms, corresponding to Swerling I and Swerling II target models, respectively. $\chi_{qk} = \beta_k \exp\left(j\left(q-1\right) f_k\right)$ is defined for the Swerling I target model, in which f_k is the Doppler frequency of the k-th target, $\exp\left(j\left(q-1\right) f_k\right)$ corresponds to the Doppler effect coefficient of the k-th target for the q-th pulse period, and β_k is the RCS coefficient of the k-th target for all Q pulse periods. This means that the RCS coefficients are invariant during the CPI. For the Swerling II target model, $\chi_{qk} = \beta_{qk} \exp\left(j\left(q-1\right) f_k\right)$, where β_{qk} is the RCS coefficient of the k-th target for the q-th pulse period, which means that the RCS coefficients change with pulses.

3.1. Constructed Tensor Model

The transmitted signals for different pulses are designed to be the same, i.e., $\mathbf{S}_q = \mathbf{S}$ for all $q = 1, \ldots, Q$. Therefore, Equation (22) can be further written as

$$
\begin{aligned}
\mathbf{Y}_q &= \sum_{k=1}^{K} \chi_{qk} \mathbf{a}_\mathrm{R}(\phi_{\mathrm{R},k}) \tilde{\mathbf{a}}_\mathrm{T}^\mathrm{T}(\phi_{\mathrm{T},k}) + \mathbf{V}_q \\
&= \mathbf{A}_\mathrm{R}(\phi_\mathrm{R}) \operatorname{diag}(\mathbf{c}_q) \tilde{\mathbf{A}}_\mathrm{T}^\mathrm{T}(\phi_\mathrm{T}) + \mathbf{V}_q
\end{aligned}
\tag{23}
$$

where $\tilde{\mathbf{a}}_\mathrm{T}(\phi_{\mathrm{T},k}) = \mathbf{S}^\mathrm{T} \mathbf{a}_\mathrm{T}(\phi_{\mathrm{T},k})$ and $\tilde{\mathbf{A}}_\mathrm{T}(\phi_\mathrm{T}) = \mathbf{S}^\mathrm{T} \mathbf{A}_\mathrm{T}(\phi_\mathrm{T}) \in \mathbb{C}^{L \times K}$. $\mathbf{c}_q = [\chi_{q1}, \cdots, \chi_{qK}]^\mathrm{T} \in \mathbb{C}^{K \times 1}$ is a column vector. For notational conciseness, $\tilde{\mathbf{A}}_\mathrm{T}$ and $\mathbf{A}_\mathrm{R}$ are used to represent $\tilde{\mathbf{A}}_\mathrm{T}(\phi_\mathrm{T})$ and $\mathbf{A}_\mathrm{R}(\phi_\mathrm{R})$, respectively. Let us define $\mathbf{C} = \begin{bmatrix} \mathbf{c}_1 & \ldots & \mathbf{c}_Q \end{bmatrix}^\mathrm{T} \in \mathbb{C}^{Q \times K}$. Equation (23) then becomes

$$
\mathbf{Y}_q = \mathbf{A}_\mathrm{R} D_q(\mathbf{C}) \tilde{\mathbf{A}}_\mathrm{T}^\mathrm{T} + \mathbf{V}_q.
\tag{24}
$$

According to [29], the following PARAFAC model is constructed after stacking $\mathbf{Y}_q$ for all $q = 1, \ldots, Q$:

$$
\underline{\mathbf{Y}} = \sum_{k=1}^{K} \mathbf{a}_\mathrm{R}(\phi_{\mathrm{R},k}) \circ \tilde{\mathbf{a}}_\mathrm{T}(\phi_{\mathrm{T},k}) \circ \mathbf{c}_k + \underline{\mathbf{V}}
\tag{25}
$$

where $\mathbf{c}_k \in \mathbb{C}^{Q \times 1}$ is the k-th column of $\mathbf{C}$, $\underline{\mathbf{Y}} \in \mathbb{C}^{M_\mathrm{R} \times L \times Q}$ and $\underline{\mathbf{V}} \in \mathbb{C}^{M_\mathrm{R} \times L \times Q}$ are third-order tensors with $\mathbf{Y}_q$ and $\mathbf{V}_q$ as their q-th matrix slice, respectively. The scalar elements $y(m, l, q)$ in tensor $\underline{\mathbf{Y}}$ can be expressed as

$$
y(m, l, q) = \sum_{k=1}^{K} a_\mathrm{R}(m, k) \tilde{a}_\mathrm{T}(l, k) c(q, k) + v(m, l, q)
\tag{26}
$$

for $m = 1, \cdots, M_\mathrm{R}$, $l = 1, \cdots, L$, and $q = 1, \cdots, Q$. $a_\mathrm{R}(m, k)$, $\tilde{a}_\mathrm{T}(l, k)$, $c(q, k)$, and $v(m, l, q)$ represent the (m, k)-th, (l, k)-th, (q, k)-th, and (m, l, q)-th scalar elements of $\mathbf{A}_\mathrm{R}$, $\tilde{\mathbf{A}}_\mathrm{T}$, $\mathbf{C}$, and $\underline{\mathbf{V}}$, respectively. The three matrix unfolded forms of this PARAFAC model can be written as

$$
\mathbf{Y}^{(1)} = (\mathbf{C} \odot \mathbf{A}_\mathrm{R}) \tilde{\mathbf{A}}_\mathrm{T}^\mathrm{T} + \mathbf{V}^{(1)}
\tag{27}
$$

$$
\mathbf{Y}^{(2)} = (\tilde{\mathbf{A}}_\mathrm{T} \odot \mathbf{C}) \mathbf{A}_\mathrm{R}^\mathrm{T} + \mathbf{V}^{(2)}
\tag{28}
$$

$$
\mathbf{Y}^{(3)} = (\mathbf{A}_\mathrm{R} \odot \tilde{\mathbf{A}}_\mathrm{T}) \mathbf{C}^\mathrm{T} + \mathbf{V}^{(3)}
\tag{29}
$$

where $\mathbf{Y}^{(1)} \in \mathbb{C}^{Q M_\mathrm{R} \times L}$, $\mathbf{Y}^{(2)} \in \mathbb{C}^{L Q \times M_\mathrm{R}}$, and $\mathbf{Y}^{(3)} \in \mathbb{C}^{M_\mathrm{R} L \times Q}$.

According to the uniqueness theorem [29], $\mathbf{A}_\mathrm{R}$, $\tilde{\mathbf{A}}_\mathrm{T}$, and $\mathbf{C}$ are unique in the presence of column permutation and scaling ambiguities if

$$
k_{\mathbf{A}_\mathrm{R}} + k_{\tilde{\mathbf{A}}_\mathrm{T}} + k_\mathbf{C} \geqslant 2(K + 1)
\tag{30}
$$

where $k_\mathbf{A}$ means the Kruskal-rank (k-rank) of $\mathbf{A}$. The composite coefficient matrix $\mathbf{C}$ has a Vandermonde structure for the Swerling I target model, but no specific structure for the Swerling II target model. Since the RCS coefficients are randomly distributed, $\mathbf{C}$ has full k-rank. The two steering matrices $\mathbf{A}_\mathrm{T}$ and $\mathbf{A}_\mathrm{R}$ have a Vandermonde structure. Since there are no special constraints on the transmitted signal waveforms, such as orthogonality, $\tilde{\mathbf{A}}_\mathrm{T}$ has no specific structure. However, it still has full k-rank because $\mathbf{S}$ is randomly generated. Therefore, $\mathbf{A}_\mathrm{R}$, $\tilde{\mathbf{A}}_\mathrm{T}$, and $\mathbf{C}$ have full k-rank. The condition expressed by Equation (30) becomes

$$
\min(M_\mathrm{R}, K) + \min(L, M_\mathrm{T}, K) + \min(Q, K) \geqslant 2(K + 1).
\tag{31}
$$

This implies that only $\min(M_T, M_R, Q) \geqslant K$ and $L \geqslant 2$ are needed to satisfy the condition expressed by Equation (31). However, MIMO radars in [20] send mutually orthogonal signals and thus require $L \geqslant M_R$, which takes up more spectral resources.

3.2. Localization via the Proposed ISR-M Method

Since the TALS algorithm is efficient and simple to implement, it is commonly used to fit tensor models, such as PARAFAC [22,29], PARATUCK2 [30], and Tucker2 [31]. However, the fitting accuracy and speed of this iterative algorithm are greatly affected by its initial value. Poor initial values can lead to poor localization results. Due to the fact that transmit and receive steering matrices $\mathbf{A}_T$ and $\mathbf{A}_R$ are invariant for different pulses during the CPI, one of $\mathbf{Y}_q$ for $q = 1, \ldots, Q$ can be used to estimate $\mathbf{A}_T$ and $\mathbf{A}_R$. Therefore, we develop a new preconditioning scheme to initialize the TALS algorithm in this subsection. This initialization scheme can also estimate the number of targets. The complete fitting process is described in Algorithm 2.

At the first stage, the received signals from one pulse period during CPI, i.e., $\mathbf{Y}_q = \mathbf{A}_R \text{diag}(\mathbf{c}_q) \tilde{\mathbf{A}}_T^T + \mathbf{V}_q$, are selected to initialize $\mathbf{A}_T$ and $\mathbf{A}_R$. Analogous to the description in Section 2, the objective problem is firstly formulated as an iterative surrogate function as shown in Equation (9). Optimal formulas for the RCS coefficient vector $\mathbf{c}_q$, DODs, and DOAs are then obtained by calculating the partial derivative, i.e., Equations (14)–(20). As described in Algorithm 1, DODs and DOAs are iteratively estimated, and the target numbers represented by K are also obtained. The transmit and receive steering matrices $\hat{\mathbf{A}}_T$ and $\hat{\mathbf{A}}_R$ are further constructed based on the estimated DODs and DOAs; hence $\hat{\tilde{\mathbf{A}}}_T = \mathbf{S}^T \hat{\mathbf{A}}_T$ is obtained.

According to the convergence condition in Algorithm 1 (i.e., the algorithm is considered to be convergent if $e^{(i)} \leqslant e_{th}$), the required number of iteration may be considerable when a small e_{th} is assumed. This setting improves estimation performance by increasing calculation cost. In this subsection, the estimation results from Algorithm 1 are utilized to initialize the TALS algorithm. As a result, there is a relatively easy requirement for accuracy. We choose a number of iteration equal to 10 in an effort to reduce computational complexity.

At the second stage, the TALS algorithm is exploited to iteratively estimate $\mathbf{A}_R$, $\tilde{\mathbf{A}}_T$, and $\mathbf{C}$. The least-square (LS) fitting formulas corresponding to Equations (27)–(29) are respectively given by

$$
\begin{aligned}
\hat{\tilde{\mathbf{A}}}_T &= \arg\min_{\mathbf{E}} \left\| \mathbf{Y}^{(1)} - (\hat{\mathbf{C}} \odot \hat{\mathbf{A}}_R) \tilde{\mathbf{A}}_T^T \right\|_F^2 \\
&= \left[(\hat{\mathbf{C}} \odot \hat{\mathbf{A}}_R)^\dagger \mathbf{Y}^{(1)} \right]^T
\end{aligned}
\tag{32}
$$

$$
\begin{aligned}
\hat{\mathbf{A}}_R &= \arg\min_{\hat{\mathbf{A}}_R} \left\| \mathbf{Y}^{(2)} - (\hat{\tilde{\mathbf{A}}}_T \odot \hat{\mathbf{C}}) \mathbf{A}_R^T \right\|_F^2 \\
&= \left[(\hat{\tilde{\mathbf{A}}}_T \odot \hat{\mathbf{C}})^\dagger \mathbf{Y}^{(2)} \right]^T
\end{aligned}
\tag{33}
$$

$$
\begin{aligned}
\hat{\mathbf{C}} &= \arg\min_{\mathbf{C}} \left\| \mathbf{Y}^{(3)} - (\hat{\mathbf{A}}_R \odot \hat{\tilde{\mathbf{A}}}_T) \mathbf{C}^T \right\|_F^2 \\
&= \left[(\hat{\mathbf{A}}_R \odot \hat{\tilde{\mathbf{A}}}_T)^\dagger \mathbf{Y}^{(3)} \right]^T.
\end{aligned}
\tag{34}
$$

The cost function with regard to $\mathbf{A}_R$, $\tilde{\mathbf{A}}_T$, and $\mathbf{C}$ are alternatively minimized until $\left| e^{(i)} - e^{(i-1)} \right| / e^{(i)} < \Delta_{th}$. It is assumed that $\Delta_{th} = 1 \times 10^{-6}$ in this paper.

Optimized initial values help to converge. Therefore, the number of iterations of the ISR-M algorithm is significantly reduced compared with the traditional TALS algorithm, which can be confirmed by Table 1.

DODs and DOAs can be extracted based on the maximum likelihood (ML) algorithm [32]. They are respectively given by

$$\hat{\phi}_{\text{T},k} = \arg\max_{\phi_{\text{T},k}} \frac{\left| \hat{\mathbf{a}}_{\text{T},k}^{\text{H}} \mathbf{S}^{\text{T}} \mathbf{a}_{\text{T}}(\phi_{\text{T},k}) \right|}{\left\| \hat{\mathbf{a}}_{\text{T},k}^{\text{H}} \right\|_2 \left\| \mathbf{S}^{\text{T}} \mathbf{a}_{\text{T}}(\phi_{\text{T},k}) \right\|_2} \tag{35}$$

$$\hat{\phi}_{\text{R},k} = \arg\max_{\phi_{\text{R},k}} \frac{\left| \hat{\mathbf{a}}_{\text{R},k}^{\text{H}} \mathbf{a}_{\text{R}}(\phi_{\text{R},k}) \right|}{\left\| \hat{\mathbf{a}}_{\text{R},k} \right\|_2 \left\| \mathbf{a}_{\text{R}}(\phi_{\text{R},k}) \right\|_2} \tag{36}$$

where $\hat{\mathbf{a}}_{\text{T},k}$ and $\hat{\mathbf{a}}_{\text{R},k}$ represent the k-th column of $\hat{\mathbf{A}}_{\text{T}}$ and $\hat{\mathbf{A}}_{\text{R}}$, and $\phi_{\text{T},k}$ and $\phi_{\text{R},k}$ are unknown parameters.

In the traditional scheme [20], the Vandermonde structure of $\mathbf{A}_{\text{T}}$ and $\mathbf{A}_{\text{R}}$ is one of the key factors in recovering angles. However, the angle extraction method in this paper takes no account of the special structure of $\mathbf{A}_{\text{T}}$ and $\mathbf{A}_{\text{R}}$ and thus is more applicable than the traditional scheme in [20].

Algorithm 2 The proposed ISR-M algorithm.

First stage:

Input: $\mathbf{Y}_q$ and $\mathbf{S}$.

Step 1.1 Apply the vec $(\cdot)$ operator to $\mathbf{Y}_q$;

Step 1.2 Set $i = 0$; Initialize the target numbers K_{init} to ensure $K < K_{\text{init}}$; Initialize $\hat{\theta}_{\text{T}}^{(0)}$, $\hat{\theta}_{\text{R}}^{(0)}$, $\hat{\mathbf{c}}^{(0)}$, and $\hat{R}^{(0)}$;

Step 1.3 For $i = 1, \ldots, I_{\max}$

    Step 1.3.1 Update the angle estimation $\hat{\theta}_{\text{T}}^{(i)}$ and $\hat{\theta}_{\text{R}}^{(i)}$ using Equation (17);

    Step 1.3.2 Update $\hat{\mathbf{c}}^{(i)}$ and $\hat{R}^{(i)}$ by Equations (15) and (16), respectively;

Step 1.4 End for

Step 1.5 Prune $\hat{\beta}_k$ when $\hat{\beta}_k < \beta_{\text{th}}$, where β_{th} is a threshold.

Output: $\hat{K}$, $\hat{\theta}_{\text{T}}$, and $\hat{\theta}_{\text{R}}$.

....

Construct $\hat{\mathbf{A}}_{\text{T}}$ and $\hat{\mathbf{A}}_{\text{R}}$ from Equations (1) and (3);

Calculate $\hat{\tilde{\mathbf{A}}}_{\text{T}} = \mathbf{S}^{\text{T}} \hat{\mathbf{A}}_{\text{T}}$.

....

Second stage :

Input: $\hat{\tilde{\mathbf{A}}}_{\text{T}}$, $\hat{\mathbf{A}}_{\text{R}}$, $\mathbf{Y}^{(1)}$, $\mathbf{Y}^{(2)}$, and $\mathbf{Y}^{(3)}$.

Step 2.1 Set $i = 0$, $\hat{\mathbf{A}}_{\text{R}}^{(0)} = \hat{\mathbf{A}}_{\text{R}}$, $\hat{\tilde{\mathbf{A}}}_{\text{T}}^{(0)} = \hat{\tilde{\mathbf{A}}}_{\text{T}}$;

Step 2.2 $i = i + 1$;

Step 2.3 Calculate the LS estimate of $\mathbf{C}$:

$$\hat{\mathbf{C}}^{(i)} = \left[(\hat{\mathbf{A}}_{\text{R}}^{(i-1)} \odot \hat{\tilde{\mathbf{A}}}_{\text{T}}^{(i-1)})^{\dagger} \mathbf{Y}^{(3)} \right]^{\text{T}};$$

Step 2.4 Calculate the LS estimate of $\tilde{\mathbf{A}}_{\text{T}}$:

$$\hat{\tilde{\mathbf{A}}}_{\text{T}}^{(i)} = \left[(\hat{\mathbf{C}}^{(i)} \odot \hat{\mathbf{A}}_{\text{R}}^{(i-1)})^{\dagger} \mathbf{Y}^{(1)} \right]^{\text{T}};$$

Step 2.5 Calculate the LS estimate of $\mathbf{A}_{\text{R}}$:

$$\hat{\mathbf{A}}_{\text{R}}^{(i)} = \left[(\hat{\tilde{\mathbf{A}}}_{\text{T}}^{(i)} \odot \hat{\mathbf{C}}^{(i)})^{\dagger} \mathbf{Y}^{(2)} \right]^{\text{T}};$$

Step 2.6 Calculate $e^{(i)} = \left\| \mathbf{Y}^{(1)} - (\hat{\mathbf{C}}^{(i)} \odot \hat{\mathbf{A}}_{\text{R}}^{(i)}) \hat{\tilde{\mathbf{A}}}_{\text{T}}^{(i)\text{T}} \right\|_{\text{F}}^2$;

Step 2.7 Repeat **Step 2.2**-**Step 2.6** until $\left| e^{(i)} - e^{(i-1)} \right| \big/ e^{(i)} < \Delta_{\text{th}}$.

Output: $\hat{\tilde{\mathbf{A}}}_{\text{T}}$, $\hat{\mathbf{A}}_{\text{R}}$, and $\hat{\mathbf{C}}$.

....

Estimate $\hat{\phi}_{\text{T},k}$ and $\hat{\phi}_{\text{R},k}$ for all $k = 1, \ldots, K$ according to Equations (35) and (36).

---

4. Simulation Results

The performance of the two proposed target localization methods is studied in this section. Define the root mean square error (RMSE) [11–14,16] as

$$\text{RMSE} = \frac{1}{K} \sum_{k=1}^{K} \sqrt{\frac{1}{N} \sum_{n=1}^{N} \left[\left(\hat{\theta}_{\text{T},k,n} - \theta_{\text{T},k}\right)^2 + \left(\hat{\theta}_{\text{R},k,n} - \theta_{\text{R},k}\right)^2 \right]} \qquad (37)$$

where N is the number of Monte Carlo simulations, and $\hat{\theta}_{\text{T},k,n}$ and $\hat{\theta}_{\text{R},k,n}$ denote the estimated values of $\theta_{\text{T},k}$ and $\theta_{\text{R},k}$ for the n-th Monte Carlo trial, respectively. For each Monte Carlo simulation, the RCS fading coefficients are randomly regenerated, while the DODs and DOAs remain constant. Throughout the simulations, we assume that the number of transmit antennas and receive antennas are equal, i.e., $M_{\text{T}} = M_{\text{R}} = J$.

4.1. Single-Pulse Bistatic MIMO Radar

In this subsection, we focus on the single-pulse bistatic MIMO radar. In order to ensure that the proposed ISR-S method can effectively and efficiently localize all targets, the condition $\min(J, L) > K$ needs to be met. A larger $\min(J, L)$ with a certain K means a better localization performance and a lower convergence speed.

Each element of **c**, i.e., the RCS coefficient β_k for all $k = 1, \ldots, K$, is randomly drawn from a Gaussian distribution with zero mean and unit variance. β_{th} is a small value that defines the range of $\hat{\beta}_k$. Therefore, we reasonably set $\beta_k \geqslant 0.02$, i.e., $\beta_{\text{th}} = 0.02$, which means that we regard $\hat{\beta}_k$ as noise and prune it if $\hat{\beta}_k < \beta_{\text{th}}$. The carrier frequency f_{c} is equal to 1 *GHZ*, and the wavelength λ is equal to $3 \times 10^8 / f_{\text{c}}$ in meters. The spacing of two adjacent antennas for the transmit and receive antenna arrays is equal to half-wavelength $\lambda/2$. The transmitted waveform matrix **S** is generated by a complex Gaussian random matrix with zero mean and unit variance by default. The SNR is defined as $\text{SNR} = 10\log 10 \left(\|\mathbf{x}\|_2^2 / \|\mathbf{v}\|_2^2 \right)$ dB for the single-pulse configuration, in which $\mathbf{x} = \left(\mathbf{S}^{\text{T}} \otimes \mathbf{I}_{M_{\text{R}}}\right) \left(\mathbf{A}_{\text{T}} \odot \mathbf{A}_{\text{R}}\right) \mathbf{c}$. The error tolerance e_{th} is set to 1×10^{-10} for a given target numbers.

In the first example, we assess the target localization performance of the proposed ISR-S method with unknown target numbers. The DODs and DOAs are $(-70°, -55°)$, $(-30°, -15°)$, $(15°, 30°)$, and $(60°, 80°)$. The rest system parameters are $K = 4$, SNR $= 20$dB, $J = 5$, and $L = 12$. As shown in Figure 2, we can clearly see that our proposed algorithm can localize all targets accurately and estimate DODs and DOAs effectively. In addition, its performance is well even with low sampling numbers, i.e., $L = 24$.

In the second example, we compare the proposed ISR-S method with existing Capon, MUSIC, and ESPRIT methods through Monte Carlo simulations with given target numbers, where $K = 3$ and $N = 500$. Figures 3 and 4 show the impact of different sampling numbers L and antenna numbers J on the RMSE performance for the above methods, respectively. To ensure that Capon, MUSIC, and ESPRIT algorithms work, orthogonal transmitted waveforms are considered in this example. In addition, the angular resolution of Capon and MUSIC algorithms is set as $0.001°$ for a fair comparison. However, such a small step size greatly increases the complexity. In order to save time to some degree, we look for all peaks in two stages. At the first stage, a scanning step size of $1°$ is chosen to find K peaks. At the second stage, we refine the angle estimation around these K peaks with a step size of $0.001°$. It can be seen in Figures 3 and 4 that the RMSE of all methods decreases as L and J increase, and the proposed super-resolution method is superior to existing methods when the SNR is above a certain threshold. The Capon and MUSIC methods cannot accurately localize all targets at each Monte Carlo run and thus results in a poor angle estimation performance at a low SNR. Their performance is also greatly sensitive to sampling numbers, represented by L, and antenna numbers, represented by J. Though the ESPRIT method has better performance than the Capon and MUSIC methods, there is still a large gap between the ESPRIT method and the proposed ISR-S method. At an RMSE of 1×10^{-3}, the

gap between the ESPRIT method and the proposed ISR-S method is about 3.3 dB for $L = 32, 128$ and 3.9 dB for $J = 8, 12$.
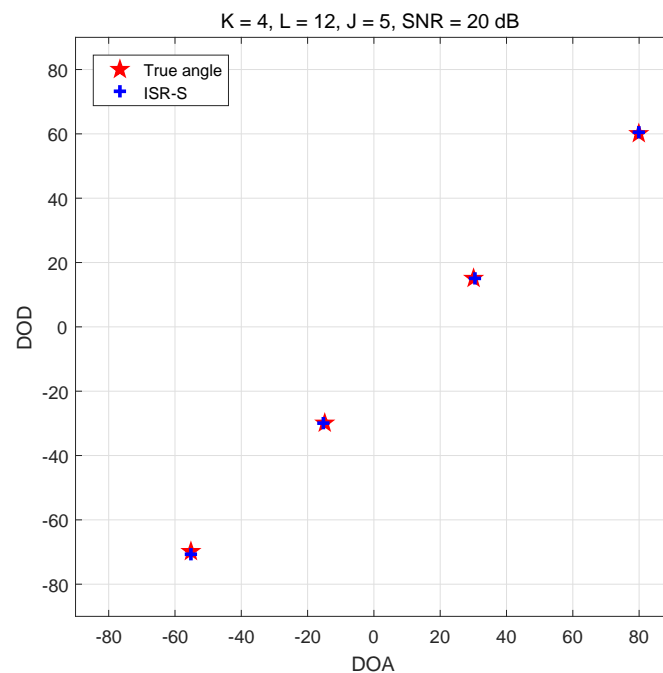

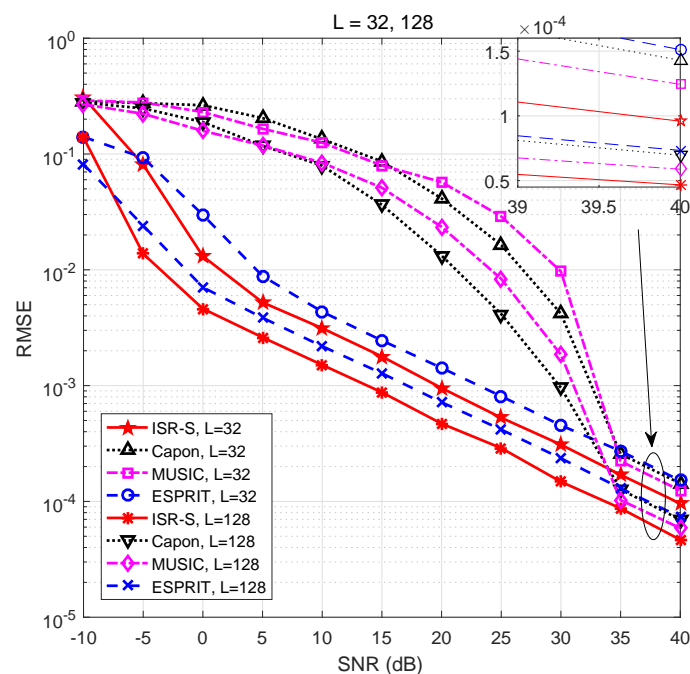**Figure 2.** Target localization performance of the proposed ISR-S method, $K = 4$ is unknown.

Figure 3. Comparison with existing MIMO radar target localization methods for different sampling numbers L, $J = 8$.

In the third example, we study the influence of the proposed ISR-S method for different target numbers through Monte Carlo simulations, where $L = 24$, $J = 12$, and $N = 500$. In particular, we consider the case that the number of targets is unknown. The proposed ISR-S method is carried out

following Algorithm 1 with $e_{th} = 1 \times 10^{-5}$, 1×10^{-4}, 1×10^{-3} and $K_{init} = 6, 9, 12$ for $K = 2, 3, 4$, respectively. The existing Capon, MUSIC, and ESPRIT methods cannot work in this case. It can be seen in Figure 5 that the RMSE performance of the proposed ISR-S method is improved as K decreases in both cases of known and unknown target numbers. We can also observe in Figure 5 that the proposed method still has high estimation accuracy above an SNR threshold even with unknown target numbers and low sampling numbers, i.e., $L = 24$.
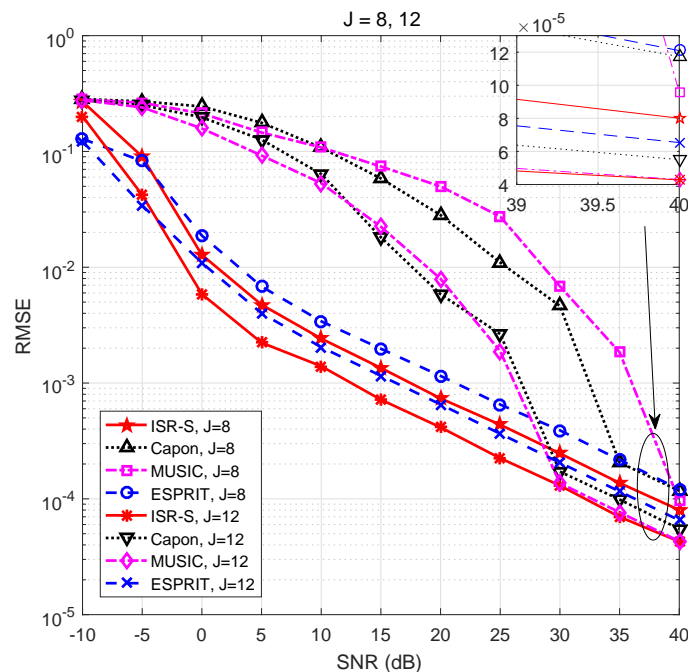
Figure 4. Comparison with existing MIMO radar target localization methods for different antenna numbers J, $L = 48$.
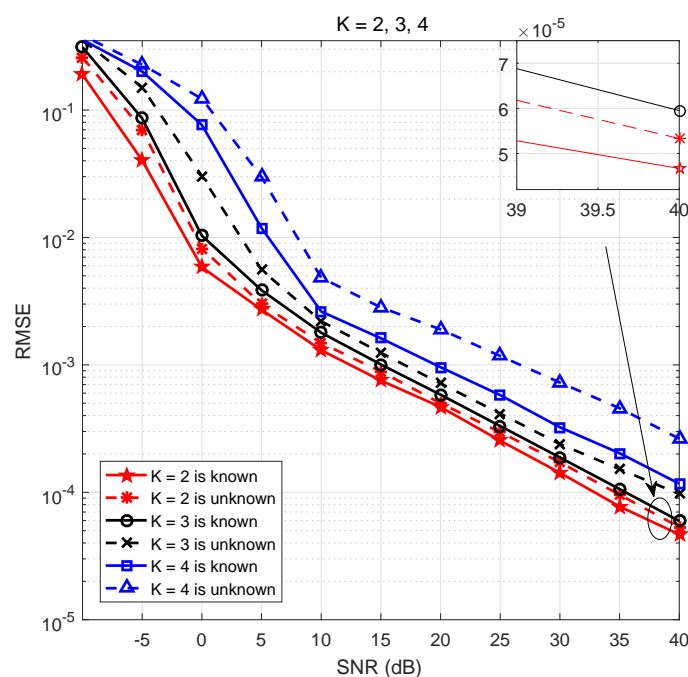
Figure 5. RMSE performance of the proposed ISR-S method for different target numbers, represented by K.

4.2. Mutiple-Pulse Bistatic MIMO Radar

In this subsection, we focus on the multiple-pulse bistatic MIMO radar. According to the uniqueness theorem of the PARAFAC model, $\min(J, Q) \geqslant K$ and $L \geqslant 2$ should be met for the second stage of our proposed ISR-M method. Meanwhile, $\min(J, L) > K$ should be met for the first stage of the ISR-M method. Therefore, $\min(J, L, Q) > K$ and $L \geqslant 2$ are needed to be met for effectively and efficiently localizing all targets in this configuration.

For the Swerling I target model, the RCS coefficient β_k is randomly drawn from a Gaussian distribution with zero mean and variance $\sigma^2_{\beta_k}$.; for the Swerling II target model, β_{qk} for all $q = 1, \ldots, Q$ are randomly drawn from a Gaussian distribution with zero mean and variance $\sigma^2_{\beta_k}$. As in Section 4.1, we also set $\beta_{\mathrm{th}} = 0.02$. The Dopper frequency f_k is equal to $2\pi v_k T_p / \lambda$, in which v_k is the velocity of the k-th target, T_p is the period of the q-th pulse and is equal to 5×10^6 in seconds. The Swerling II target model is chosen, and the SNR is defined as $\mathrm{SNR} = 10\log10 \left(\sum\limits_{q=1}^{Q} \|\mathbf{X}_q\|_{\mathrm{F}}^2 \Big/ \sum\limits_{q=1}^{Q} \|\mathbf{V}_q\|_{\mathrm{F}}^2 \right)$ dB for the multiple-pulse configuration, in which $\mathbf{X}_q = \mathbf{A}_{\mathrm{R}}\mathrm{diag}\left(\mathbf{c}_q\right) \tilde{\mathbf{A}}_{\mathrm{T}}^{\mathrm{T}}$. The other system parameters are set as in the last subsection.

In the first example, we assess the target localization performance of the proposed ISR-M method with unknown target numbers, in which $K = 4$ and $Q = 8$. In particular, we compare the case of $J > K$ and $J = K$. The rest of the system parameters are the same as the first example in the previous subsection. As shown in Figures 6 and 7, we can clearly see that our proposed ISR-M algorithm can estimate DODs and DOAs effectively, and accurate localization is also achieved when $J = K$, even with unknown target numbers and low sampling numbers.
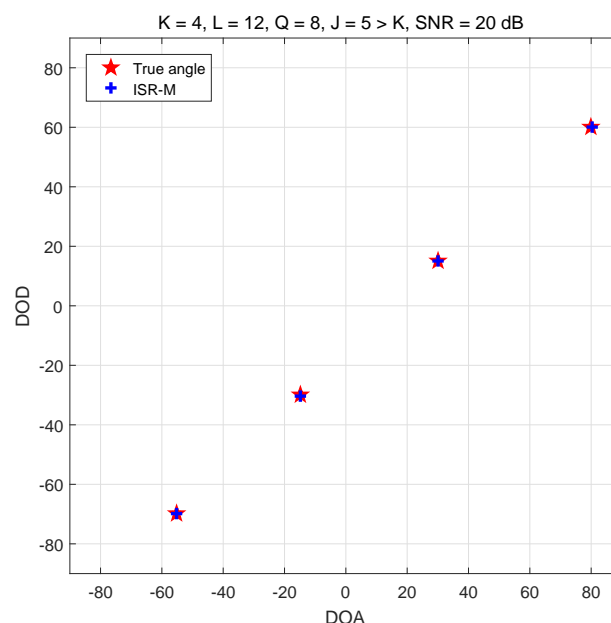
Figure 6. Target localization performance of the proposed ISR-M method, $J = 5 > K = 4$.

In the second example, we compare the RMSE performance of the proposed ISR-M method with that of existing Capon, MUSIC, and ESPRIT methods for different L, Q, and J values through Monte Carlo simulations with given target numbers, where $K = 3$ and $N = 500$. In particular, the RMSE curves of the proposed ISR-S algorithm are also plotted in this example. An angular resolution identical to that in the second example of the previous subsection is chosen for Capon and MUSIC algorithms. For the ISR-S method (or the first stage of the ISR-M method), the main computational cost in each iteration rests with computing the gradient in Step 3 (or Step 1.3.1). The computational complexity for computing the gradient in each iteration is $O\left(L\left(M_{\mathrm{R}} + M_{\mathrm{T}}\right) K^2\right)$. For

the second stage of the ISR-M method, the computational complexity in each iteration for Step 2.3, 2.4, and 2.5 are $O\left(LM_RK^2\right) + QKLM_R$, $O\left(QM_RK^2\right) + QKLM_R$, and $O\left(LQK^2\right) + QKLM_R$, respectively. Therefore, the overall computational cost is $O\left(\left(2LM_R + LM_T + QM_R + LQ\right)K^2\right) + 3QKLM_R$ for the ISR-M method. For Capon and MUSIC methods, a small scanning step size is usually chosen to improve the angular resolution in practice, which means that the required iteration number is greatly increased in order to achieve a localization accuracy identical to that of other algorithms. Therefore, their complexity is usually higher than the proposed ISR-S and ISR-M methods. Since the ESPRIT method does not involve iterations, its complexity is the lowest among these methods. Comparing Figures 8–11, we can clearly see that the estimation performance of all methods except ISR-S is improved as *L*, *Q*, and *J* increase. Note that, because only one pulse-period-received information is used, the performance of the proposed ISR-S algorithm is not sensitive to *Q* and only affected by *L* and *J*. However, the proposed ISR-S method still shows better localization performance than the Capon and MUSIC algorithms at a low SNR. It can also be seen that the proposed ISR-M method invariably outperforms existing methods regardless of *L*, *Q*, and *J*. Even in the case of a high SNR, in which the MUSIC algorithm shows better performance than the ESPRIT algorithm, there is always a gap of at least 6.5 dB between the ISR-M method and the MUSIC method.
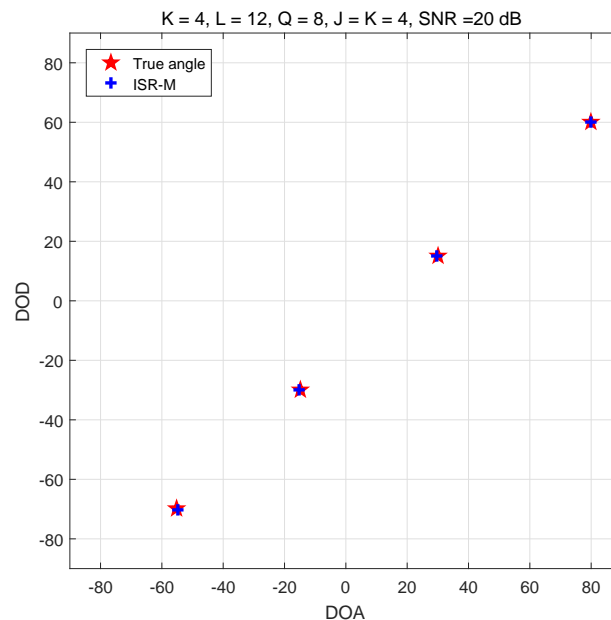
Figure 7. Target localization performance of the proposed ISR-M method, *J* = *K* = 4.
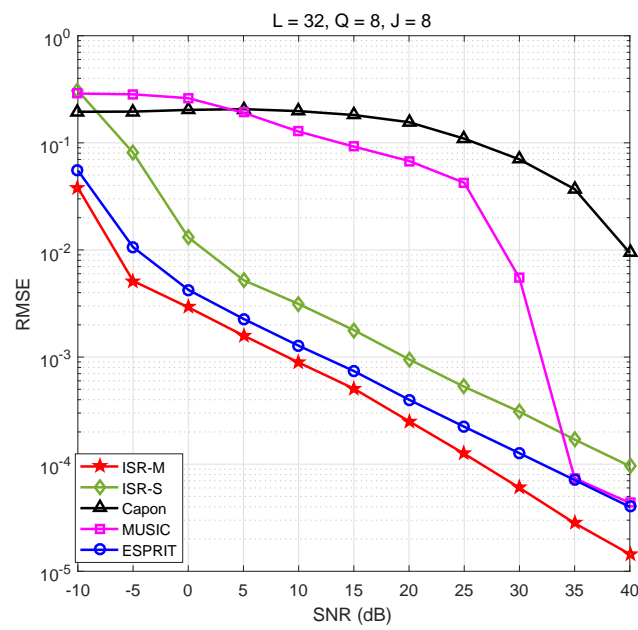
Figure 8. Comparison with existing MIMO radar target localization methods with $K = 3$, $L = 32$, $Q = 8$, and $J = 8$.
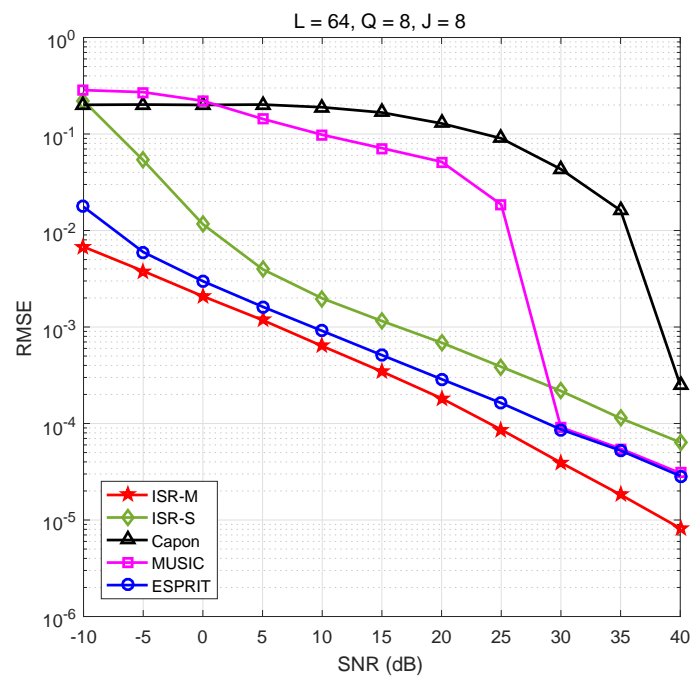

Figure 9. Comparison with existing MIMO radar target localization methods with $K = 3$, $L = 64$, $Q = 8$, and $J = 8$.
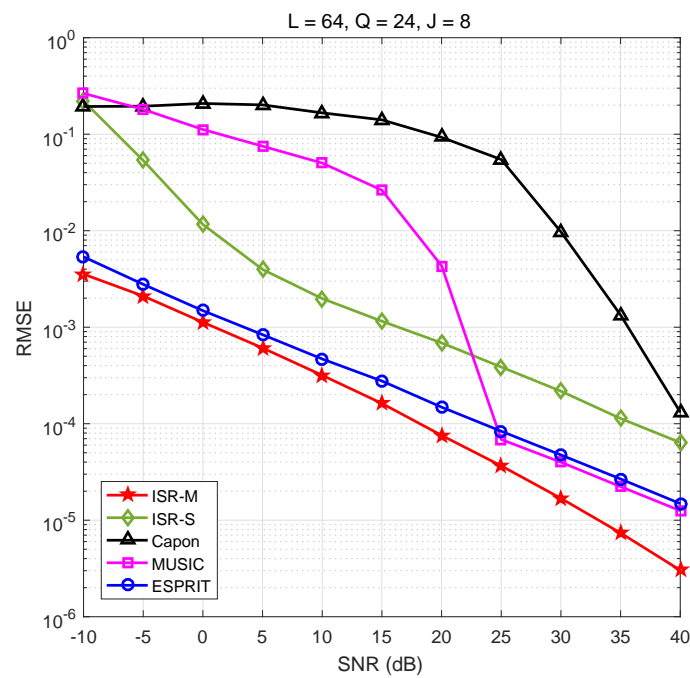
Figure 10. Comparison with existing MIMO radar target localization methods with $K = 3$, $L = 64$, $Q = 24$, and $J = 8$.
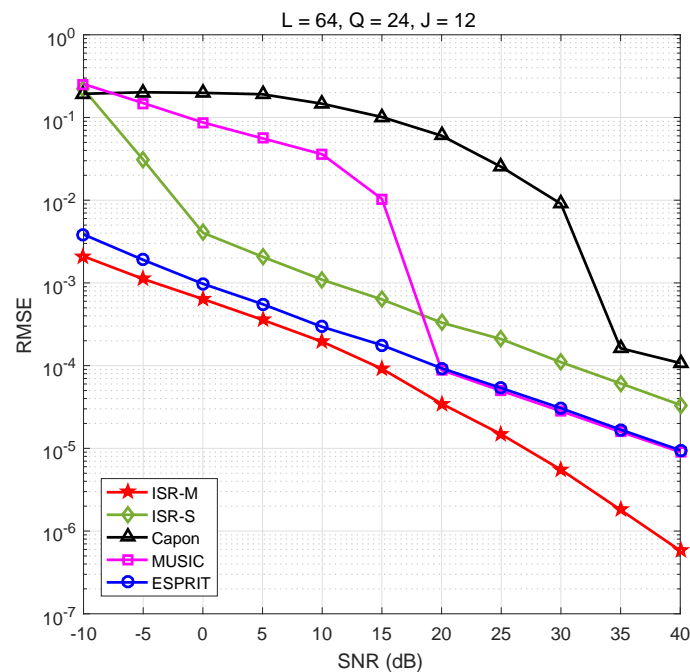

Figure 11. Comparison with existing MIMO radar target localization methods with $K = 3$, $L = 64$, $Q = 24$, and $J = 12$.

In the third example, we compare the average iteration number of the proposed ISR-M method and the traditional TALS method through Monte Carlo simulations with the same parameters as in the second example. The traditional TALS algorithm is susceptible to poor initial values, which results in poor estimation performance. Its RMSE curve versus the SNR is thus not analyzable for N Monte Carlo trials and not plotted in the second example. The proposed ISR-M algorithm greatly improves

the stability of the TALS algorithm without any loss of estimation accuracy. Moreover, as shown in Table 1, the average iteration number of the ISR-M algorithm is about half of the TALS algorithm, which means that the computational complexity of ISR-M is greatly reduced.

Table 1. Comparison of average iteration number for the proposed ISR-M method and the traditional TALS method.

SNR (dB)	−10	−5	0	5	10	15	20	25	30	35	40
$L = 32, Q = 8, J = 8$											
ISR − M	31	9	6	6	6	7	7	8	8	9	9
TALS	59	23	16	22	15	54	20	16	28	32	14
$L = 64, Q = 8, J = 8$											
ISR − M	23	7	6	6	7	7	8	8	8	9	9
TALS	26	19	18	18	26	20	31	20	25	35	31
$L = 64, Q = 24, J = 8$											
ISR − M	9	6	5	5	5	5	5	6	6	6	6
TALS	17	13	15	18	12	22	17	14	19	19	17
$L = 64, Q = 24, J = 12$											
ISR − M	10	7	4	4	4	5	5	5	6	6	6
TALS	12	14	14	14	16	14	14	18	14	16	16

5. Conclusions

We have proposed two target localization methods based on iterative super-resolution for the bistatic MIMO radar. Both of our proposed methods can be used for accurate multiple targets localization even if the number of targets is unknown. Compared with the existing Capon, MUSIC, and ESPRIT methods, the two proposed methods have better DOD/DOA estimation performance. In addition, the proposed ISR-M method shows a more stable performance and a higher convergence speed than the traditional TALS algorithm. Simulation results verify the efficacy and accuracy of the two proposed target localization methods. Perspectives of this work include an extension to multiple-pulse multi-static radar systems. In this configuration, the received pulses can be expressed as a block-component-decomposition (BCD) [33] model. We will deduce new identifiability and uniqueness conditions, and develop new efficient target localization algorithms. The imaging technique will also be developed in multi-static configurations [34]. In addition, a theoretical resolution [35] and the minimal separation angles analyses of radar systems will be taken into account in our future works.

References

1. He, Q.; Wang, Z.; Hu, J.; Blum, R.S. Performance gains from cooperative MIMO radar and MIMO communication systems. *IEEE Signal Process. Lett.* **2019**, *26*, 194–198. [CrossRef]

2. Aittomäki, T.; Koivunen, V. Mismatched filter design and interference mitigation for MIMO radars. *IEEE Trans. Signal Process.* **2016**, *65*, 454–466. [CrossRef]

3. Yang, P.; Yang, H. Optimal Linear Detection for MIMO Systems with Finite Constellation Inputs. *IEEE Signal Process. Lett.* **2019**, *26*, 612–616. [CrossRef]

4. Wang, P.; Li, H.; Himed, B. A parametric moving target detector for distributed MIMO radar in non-homogeneous environment. *IEEE Trans. Signal Process.* **2013**, *61*, 2282–2294. [CrossRef]

5. Urco, J.M.; Chau, J.L.; Weber, T.; Vierinen, J.P.; Volz, R. Sparse signal recovery in MIMO specular meteor radars with waveform diversity. *IEEE Trans. Geosci. Remote Sens.* **2019**, *57*, 10088–10098. [CrossRef]

6. Chiriyath, A.R.; Paul, B.; Jacyna, G.M.; Bliss, D.W. Inner bounds on performance of radar and communications co-existence. *IEEE Trans. Signal Process.* **2015**, *64*, 464–474. [CrossRef]

7. Chiriyath, A.R.; Paul, B.; Bliss, D.W. Radar-communications convergence: Coexistence, cooperation, and co-design. *IEEE Trans. Cognit. Commun. Netw.* **2017**, *3*, 1–12. [CrossRef]

8. Godrich, H.; Haimovich, A.M.; Blum, R.S. Target localization accuracy gain in MIMO radar-based systems. *IEEE Trans. Inf. Theory* **2010**, *56*, 2783–2803. [CrossRef]

9. Gao, X.; Zhang, X.; Feng, G.; Wang, Z.; Xu, D. On the MUSIC-derived approaches of angle estimation for bistatic MIMO radar. In Proceedings of the 2009 International Conference on Wireless Networks and Information Systems, Shanghai, China, 28–29 December 2009; pp. 343–346.

10. Xie, R.; Liu, Z.; Wu, J.X. Direction finding with automatic pairing for bistatic MIMO radar. *Signal Process.* **2012**, *92*, 198–203. [CrossRef]

11. Zhang, X.; Xu, L.; Xu, L.; Xu, D. Direction of departure (DOD) and direction of arrival (DOA) estimation in MIMO radar with reduced-dimension MUSIC. *IEEE Commun. Lett.* **2010**, *14*, 1161–1163. [CrossRef]

12. Xu, J.; Wang, W.Q.; Gui, R. Computational Efficient DOA, DOD, and Doppler Estimation Algorithm for MIMO Radar. *IEEE Signal Process. Lett.* **2018**, *26*, 44–48. [CrossRef]

13. Zhang, X.; Xu, D. Angle estimation in MIMO radar using reduced-dimension Capon. *Electron. Lett.* **2010**, *46*, 860–861. [CrossRef]

14. Zhang, X.; Xu, D. Angle estimation in bistatic MIMO radar using improved reduced dimension Capon algorithm. *J. Syst. Eng. Electron.* **2013**, *24*, 84–89. [CrossRef]

15. Ciuonzo, D.; Romano, G.; Solimene, R. Performance analysis of time-reversal MUSIC. *IEEE Trans. Signal Process.* **2015**, *63*, 2650–2662. [CrossRef]

16. Tan, J.; Nie, Z.; Wen, D. Low complexity MUSIC-based direction-of-arrival algorithm for monostatic MIMO radar. *Electron. Lett.* **2017**, *53*, 275–277. [CrossRef]

17. Duofang, C.; Baixiao, C.; Guodong, Q. Angle estimation using ESPRIT in MIMO radar. *Electron. Lett.* **2008**, *44*, 770–771. [CrossRef]

18. Zheng, G.; Chen, B.; Yang, M. Unitary ESPRIT algorithm for bistatic MIMO radar. *Electron. Lett.* **2012**, *48*, 179–181. [CrossRef]

19. Zheng, G.; Tang, J.; Yang, X. ESPRIT and unitary ESPRIT algorithms for coexistence of circular and noncircular signals in bistatic MIMO radar. *IEEE Access* **2016**, *4*, 7232–7240. [CrossRef]

20. Nion, D.; Sidiropoulos, N.D. Tensor algebra and multidimensional harmonic retrieval in signal processing for MIMO radar. *IEEE Trans. Signal Process.* **2010**, *58*, 5693–5705. [CrossRef]

21. Wang, X.; Wang, W.; Liu, J.; Liu, Q.; Wang, B. Tensor-based real-valued subspace approach for angle estimation in bistatic MIMO radar with unknown mutual coupling. *Signal Process.* **2015**, *116*, 152–158. [CrossRef]

22. Xu, B.; Zhao, Y. Transmit Beamspace-Based Unitary Parallel Factor Method for DOD and DOA Estimation in Bistatic MIMO Radar. *IEEE Access* **2018**, *6*, 65573–65581. [CrossRef]

23. Fang, J.; Wang, F.; Shen, Y.; Li, H.; Blum, R.S. Super-resolution compressed sensing for line spectral estimation: An iterative reweighted approach. *IEEE Trans. Signal Process.* **2016**, *64*, 4649–4662. [CrossRef]

24. Hu, C.; Dai, L.; Mir, T.; Gao, Z.; Fang, J. Super-resolution channel estimation for mmWave massive MIMO with hybrid precoding. *IEEE Trans. Veh. Technol.* **2018**, *67*, 8954–8958. [CrossRef]

25. Li, J.; Stoica, P. MIMO radar with colocated antennas. *IEEE Signal Process. Mag.* **2007**, *24*, 106–114. [CrossRef]

26. Chen, C.Y.; Vaidyanathan, P.P. MIMO radar space–time adaptive processing using prolate spheroidal wave functions. *IEEE Trans. Signal Process.* **2008**, *56*, 623–635. [CrossRef]

27. Shen, Y.; Fang, J.; Li, H. Exact reconstruction analysis of log-sum minimization for compressed sensing. *IEEE Signal Process. Lett.* **2013**, *20*, 1223–1226. [CrossRef]

28. Candes, E.J.; Wakin, M.B.; Boyd, S.P. Enhancing sparsity by reweighted *l* 1 minimization. *J. Fourier Anal. Appl.* **2008**, *14*, 877–905. [CrossRef]

29. Sidiropoulos, N.D.; De Lathauwer, L.; Fu, X.; Huang, K.; Papalexakis, E.E.; Faloutsos, C. Tensor decomposition for signal processing and machine learning. *IEEE Trans. Signal Process.* **2017**, *65*, 3551–3582. [CrossRef]

30. Du, J.; Yuan, C.; Tian, P.; Lin, H. Channel estimation for multi-input multi-output relay systems using the PARATUCK2 tensor model. *IET Commun.* **2016**, *10*, 995–1002. [CrossRef]

31. Favier, G.; Fernandes, C.A.R.; de Almeida, A.L. Nested Tucker tensor decomposition with application to MIMO relay systems using tensor space–time coding (TSTC). *Signal Process.* **2016**, *128*, 318–331. [CrossRef]

32. Zhou, Z.; Fang, J.; Yang, L.; Li, H.; Chen, Z.; Blum, R.S. Low-rank tensor decomposition-aided channel estimation for millimeter wave MIMO-OFDM systems. *IEEE J. Sel. Areas Commun.* **2017**, *35*, 1524–1538. [CrossRef]

33. De Lathauwer, L. Decompositions of a higher-order tensor in block terms—Part I: Lemmas for partitioned matrices. *SIAM J. Matrix Anal. Appl.* **2008**, *30*, 1022–1032. [CrossRef]

34. Ciuonzo, D. On time-reversal imaging by statistical testing. *IEEE Signal Process. Lett.* **2017**, *24*, 1024–1028. [CrossRef]

35. Ciuonzo, D.; Rossi, P.S. Noncolocated time-reversal MUSIC: High-SNR distribution of null spectrum. *IEEE Signal Process. Lett.* **2017**, *24*, 397–401. [CrossRef]